PERGAMON

International Journal of Heat and Mass Transfer 41 (1998) 3131–3148

International Journal of HEAT and MASS TRANSFER

Convective cooling of a heated obstacle in a channel

Timothy J. Young and Kambiz Vafai†

Department of Mechanical Engineering, The Ohio State University, 206 West 18th Avenue, Columbus, OH 43210-1107, U.S.A.

Received 11 March 1997 and in final form 8 October 1997

Abstract

A detailed investigation of the forced convective cooling of a heated obstacle mounted upon a channel wall is presented. The Navier–Stokes equations are used to characterize the flow field surrounding the conductive obstacle. Special emphasis is given in the systematic analysis to detail the local Nusselt number distributions and mean Nusselt numbers for the individual exposed obstacle faces. The study employs parametric variations in the obstacle height and width, as well as the thermal conductivity ratio k_{solid}/k_{fluid}, flow rate (Re_{D_h}), and heating method, to detail important fundamental and practical results. Comparison with an analytical solution for thermally developing flow in a channel shows reasonable estimates to Nusselt numbers can be made by choosing an appropriate length scale. It is shown that specific choices in obstacle size, shape and thermal conductivity can produce significant effects on the flow and heat transfer characteristics.

Nomenclature

c_p specific heat at constant pressure [J $(kg^{-1} \cdot K^{-1})$]
D_h hydraulic diameter [m]
h obstacle height [m]
h_c convective heat transfer coefficient [W $(m^{-2} \cdot K^{-1})$]
H channel height [m]
k thermal conductivity [W $(m^{-1} \cdot K^{-1})$]
n normal coordinate
Nu Nusselt number, $h_c H/k_f$
p pressure [Pa]
Pe_H Péclet number, $\rho_f c_{Pf} u_m H/k_f$
Pr Prandtl number, $\mu_f c_{Pf}/k_f$
q'' heat flux [W m^{-2}]
q''' volumetric heat generation rate [W m^{-3}]
Re_H Reynolds number, $\rho_f u_m H/\mu_f$
T temperature [K]
u x-component of velocity [m s^{-1}]
v y-component of velocity [m s^{-1}]
w obstacle width [m]
x, y Cartesian coordinates.

Greek symbols
μ dynamic viscosity [(N · s) m^{-2}]
Θ dimensionless temperature $[(T-T_e)/(q''H/k_f)]$
ρ density [kg m^{-3}].

Subscripts
b bypass
f fluid
e entrance
L left surface
m mean
N iteration number
o outlet
R right surface
s solid
T top surface
w wall
x local
0 initial.

Superscript
* dimensionless.

1. Introduction

Fluid flow around bluff bodies mounted on a channel wall forms a fundamental basis for studies of the con-

† Author to whom correspondence should be addressed. Tel.: 001 614 292 6560. Fax: 001 614 292 3163/6560. E-mail: vafai.1@osu.edu.

0017–9310/98 $19.00
PII: S0017-9310(97)00323-2

vective cooling of electrical devices. This subject has received much attention as electronic system and device technology has improved and performance increases are sought [1]. As the failure rate of an individual electronic device has been statistically correlated to be proportional to the exponential of the device junction temperature, rising temperatures imply lower reliabilities [2]. Improved thermal design would increase temperature uniformity to reduce thermal stresses and local hot spots in addition to increasing the transfer of waste heat away from the package to allow increased energy throughput, faster switching, or higher operating temperatures.

Models for the cooling of electronic components have been widely studied both numerically and experimentally [3]. In most investigations the problem is idealized to the fluid flow and thermal analysis of heat generating, quadrilateral obstacles, representing the electronic devices, within a parallel plate channel. This description of the problem allows general results to be obtained in lieu of system specific results. Little analytical work exists due to the complexity of the problems and the simplifying assumptions required. Haji-Sheikh [4] found the steady-state peak temperature for a three-dimensional heat flux tube in a semiconductor with a thin heat source using the Green's function solution method. The Kirchoff transformation was used to account for the temperature dependent thermal conductivities of typical semiconductor materials. The convergence of the steady-state solution was found to be slow, with as many as two million terms required.

Numerically, investigations have been performed in two- and three-dimensions, with laminar and turbulent flows, various convective regimes, complex (system specific) or simple (homogeneous and isotropic) modules, and individual or arrays of obstacles. Davalath and Bayazitoglu [5] solved the two-dimensional, conjugate heat transfer problem for laminar flow over an array of three obstacles with uniform conductivity and volumetric heat generation. Utilizing a control volume formulation, obstacle mean Nusselt numbers were correlated via equations of the form $\overline{Nu}_m = a\ Re^b\ Pr^c$. The spacing between the obstacles was also varied between one and two times the obstacle length. The resultant inter-obstacle flow patterns, resembling the classic driven cavity, were driven by the core fluid flowing over the obstacles. Zebib and Wo [6] investigated forced air cooling of a single, two-dimensional, internally complex, multiconductivity obstacle within a channel. The channel walls were modeled as copper-encased epoxy glass boards with convective cooling (h_c = const.) beneath the lower channel wall. Their approach allows the investigation of internal module design changes on the thermal transport within and outside the module, but are strictly limited to the given geometry. Nigen and Amon [7] employed the spectral element method to study the conjugate heat transport from a single obstacle with local or uniform heat generation and single or multiple materials. Huang and Vafai [8] investigated the enhancement of forced convective flow and thermal characteristics using various arrangements of multiple porous obstacles in a channel with the Brinkman–Forchheimer-extended Darcy model. Substantial periodicity, vortex control, and large increases in Nusselt number were demonstrated through alteration of governing physical parameters.

In order to circumvent the limitations of shape-based Reynolds number scaling, as detailed by Moffat and Ortega [9], parametric analyses are customarily performed. These results provide bounds for system specific studies as well as furnishing insight into the prevailing physical processes. Yang and Yang [10], employing the control volume method, studied turbulent, two-dimensional channel flow with one and two obstacles. These obstacles were both short (height from 1/5–1/15 of the channel height) and widely spaced (fifteen times the channel height). The bottom wall was held at a constant temperature downstream of the modules and the effect upon heat transfer of the reattachment point was investigated. The turbulent flow over an internally complex, two-dimensional obstacle was studied by Wietrzak and Poulikakos [11]. The effects of variations in obstacle height and distance from the channel entrance, composition of the obstacle internal sections, heated section size, and flow rate were found. Increases in the obstacle height strengthened fluid recirculations before, after, and upon the top surface of the obstacle, thus increasing the obstacle Nusselt number. Choi *et al.* [12] numerically investigated the effects of varying the thermal conductivity of the circuit board upon which heated obstacles were mounted. They found that the effectiveness of highly conductive circuit boards was strongly dependent on the obstacle spacing.

Jubran *et al.* [13] reported experimental investigations into the effect of rectangular and noncubical obstacles of various lengths, widths, and heights on pressure drop and heat transfer enhancement. It was found that changes in obstacle size or shape can lead to Nusselt number increases as high as 40%. These studies expanded upon the works of Sparrow and coworkers [14, 15] who utilized the naphthalene sublimation technique to examine the effects of missing obstacles, barriers, and height differences on arrays of square obstacles. Mass transfer enhancements of up to two times were measured resulting from the perturbations of the uniform arrays. Nakayama and Park [16] experimentally investigated the three-dimensional transport from the floor area near a heated obstacle and found complex temperature and heat transfer distributions. The flow structure and mean heat transfer characteristics around single, two- and three-dimensional heated obstacles in a channel was studied by Roeller *et al.* [17] using laser doppler velocimetry. Increases in mean Nusselt number were found for decreasing channel height due to a greater vena contracta

effect. Decreases in obstacle width also increased the mean heat transfer due to more intense three-dimensional transport and turbulent intensity. Other experimental examinations into the effects of obstacle array non-uniformities include Lehmann and Wirtz [18], who varied obstacle length and spacing, and Garimella and Eibeck [19], varying channel height and spanwise obstacle spacing.

In this work, a systematic and thorough investigation of forced convective cooling of an individual heated obstacle mounted upon an insulated channel wall is presented. A wide ranging series of parametric alterations is employed to establish the important fundamental effects and provide practical results. This study was motivated by the need for a coherent interpretation of results detailing the underlying physical phenomena. The influences of parametric changes in the basic obstacle geometry, Re_{D_h}, and k_s/k_f, as well as the effects of heat input method, upon the flow and heat transfer are examined. These results document the dependence of the streamline, isotherm, and Nusselt number on the governing parameters. Special emphasis is given to detail the local Nusselt number distributions and mean Nusselt numbers for the individual exposed obstacle faces. It is shown that specific choices of descriptive parameters can exert significant influence upon the flow and thermal characteristics. For example, choosing a particular obstacle shape in combination with an appropriate thermal conductivity can improve heat transfer in a local region. Small sensitivity of the flow and thermal fields is demonstrated, however, for other modifications, such as surface flux (q'') to volumetric (q''') heating or further increases in large obstacle thermal conductivities. In addition, it is shown that estimates for the Nusselt number along the obstacle top face can be made utilizing an analytical solution to the thermally developing channel flow problem.

2. Analysis

The analysis is made for steady, laminar, viscous, incompressible, Newtonian fluid flow through a two-dimensional channel with a solid obstacle on the bottom wall, as depicted in Fig. 1(a). Buoyancy induced effects are assumed negligible, weakly coupling the momentum and energy equations through the convective terms. The thermophysical properties of the fluid and solid phases are constant. Viscous heat dissipation in the fluid is assumed to be negligible compared with conduction and convection.

The continuum fluid flow problem, considering the above assumptions, is modeled utilizing the Navier–Stokes equations in Cartesian coordinates

mass conservation

$$\frac{\partial u^*}{\partial x^*}+\frac{\partial v^*}{\partial y^*}=0 \tag{1}$$

x-momentum conservation

$$Re_H\left(u^*\frac{\partial u^*}{\partial x^*}+v^*\frac{\partial u^*}{\partial y^*}\right)=-\frac{\partial p^*}{\partial x^*}+\left(\frac{\partial^2 u^*}{\partial x^{*2}}+\frac{\partial^2 u^*}{\partial y^{*2}}\right) \tag{2}$$

y-momentum conservation

$$Re_H\left(u^*\frac{\partial v^*}{\partial x^*}+v^*\frac{\partial v^*}{\partial y^*}\right)=-\frac{\partial p^*}{\partial y^*}+\left(\frac{\partial^2 v^*}{\partial x^{*2}}+\frac{\partial^2 v^*}{\partial y^{*2}}\right) \tag{3}$$

fluid phase energy conservation

$$Pe_H\left(u^*\frac{\partial \Theta_f^*}{\partial x^*}+v^*\frac{\partial \Theta_f^*}{\partial y^*}\right)=\frac{\partial^2 \Theta_f^*}{\partial x^{*2}}+\frac{\partial^2 \Theta_f^*}{\partial y^{*2}}. \tag{4}$$

The energy flow through the solid, homogeneous, and isotropic obstacle is governed by the Laplacian equation solid phase energy conservation

$$\frac{\partial^2 \Theta_s^*}{\partial x^{*2}}+\frac{\partial^2 \Theta_s^*}{\partial y^{*2}}=0. \tag{5}$$

The governing equations were cast into dimensionless form using the following

$$u^*\equiv\frac{u}{u_m},\quad v^*\equiv\frac{v}{u_m},\quad x^*\equiv\frac{x}{H},$$

$$y^*\equiv\frac{y}{H},\quad p^*\equiv\frac{pH}{\mu_f u_m}\quad \Theta^*\equiv\frac{T-T_e}{(q''H/k_f)},$$

$$Re_H\equiv\frac{\rho_f u_m H}{\mu_f},\quad Pe_H\equiv\frac{\rho_f c_{Pf} u_m H}{k_f}. \tag{6}$$

The dimensionless obstacle height and width are given, respectively, by $h^*\equiv h/H$ and $w^*\equiv w/H$. The mean velocity is given by $u_m=H^{-1}\int_0^H u(y)\,dy$. The thermal conductivity of the obstacle is k_s/k_f. The superscripts are dropped for convenience.

2.1. Boundary conditions

Due to the elliptic nature of the governing conservation equations, boundary conditions along the entire solution domain must be specified for all field variables. The fluid enters the channel at the ambient temperature with a fully developed, parabolic profile. Entrance conditions are given by

$$u=6y(1-y),\quad v=0,\quad \Theta_f=0. \tag{7}$$

At the channel outlet, zero streamwise gradients are prescribed. Furthermore, by choosing an extended computational domain, as described in Vafai and Kim [20], it was ensured that the computational outflow boundary conditions had no effect upon the physical domain solutions. The outlet boundary conditions are given as

$$\frac{\partial u}{\partial x}=0,\quad \frac{\partial v}{\partial x}=0,\quad \frac{\partial \Theta_f}{\partial x}=0. \tag{8}$$

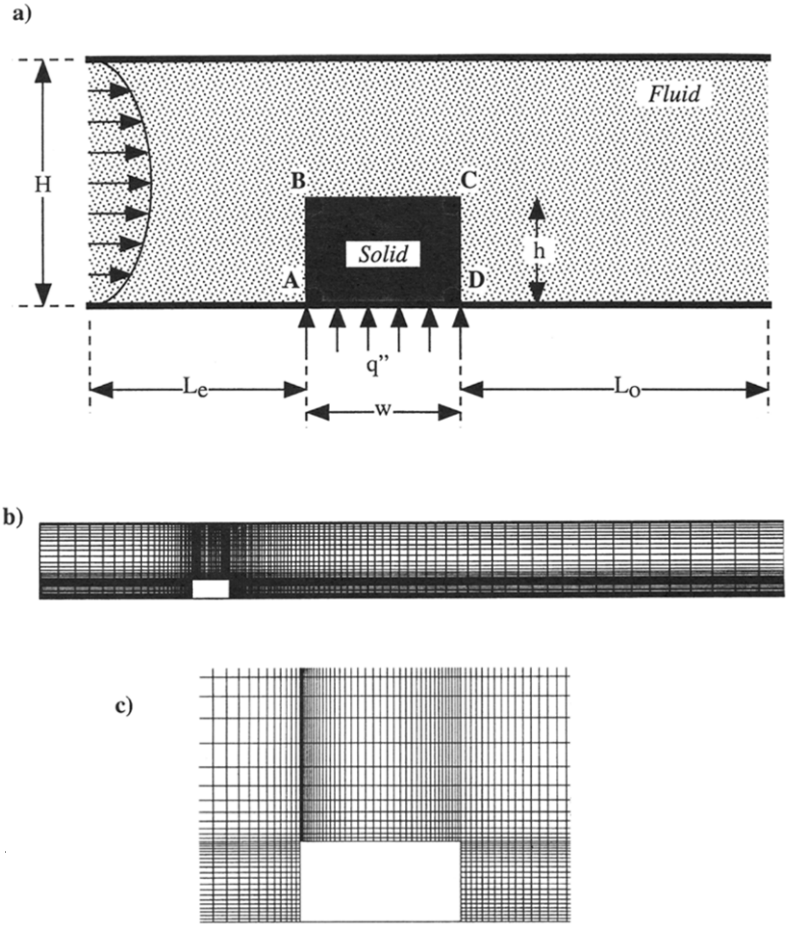

Fig. 1. (a) Schematic diagram of the single obstacle problem, (b) mesh plot of a typical computational domain, and (c) a close-up of the region near the obstacle. The mesh within the obstacle is not shown for clarity.

Both the upper and lower channel walls are insulated except at the obstacle location. At the insulated regions, $\partial\Theta_f/\partial y = 0$ and the no-slip condition, $u = 0$ and $v = 0$, prevails. The adiabatic wall condition was selected to elucidate the principal aspects of parametric changes in the heated obstacles to the flow and thermal fields within the channel. As discussed by Kim *et al.* [21], isothermal and adiabatic channel wall boundary conditions oversimplify the problem of heat transfer from powered devices to conducting circuit boards. Conjugate modeling of the channel walls, however, creates a much more system specific problem that may obscure relevant underlying details. Choi *et al.* [12] found that systems with densely populated, heat generating components do not see substantial decreases in temperature with highly conducting circuit boards.

The base of the solid obstacle receives the prescribed heat flux $q'' = 1$. At the interfaces of the fluid and the obstacle, the no-slip condition and the continuities of temperature and heat flux are accounted for

$$u = 0, \quad v = 0, \quad \Theta_f = \Theta_s, \quad k_f \frac{\partial \Theta_f}{\partial \mathbf{n}} = k_s \frac{\partial \Theta_s}{\partial \mathbf{n}}. \tag{9}$$

2.2. Numerical scheme

The Galerkin method of weighted residuals of the finite element formulation is utilized to discretize the non-linear system of governing equations and boundary conditions. The application of this technique to fluid dynamics and conjugate heat transfer problems is well documented [22].

The continuum domain is divided into a set of non-overlapping regions termed elements. Within each element the dependent variables are approximated utilizing interpolation functions in terms of the local normalized element coordinates. Nine node quadrilateral elements, with biquadratic interpolation functions, were utilized to discretize the problem domain. Substitution of the approximations into the system of governing equations and boundary conditions yields a residual for each

of the conservation equations. In the Galerkin method these residuals are reduced to zero in a weighted sense over each element volume by making them orthogonal to the interpolation functions through equations of the form $\int_{V^e}(\psi_i \cdot \mathbf{R}_i)\,dV^e = 0$, where ψ_i are the interpolation functions, $\mathbf{R}_i$ the residuals, and V^e the element volumes. This procedure yields a system of equations for each element which can be written as

$$\mathbf{K}(\mathbf{U}_x, \mathbf{U}_y, \mathbf{T})\Omega = \mathbf{F}(\mathbf{U}_x, \mathbf{U}_y, \mathbf{T}) \tag{10}$$

where $\Omega = (\mathbf{U}_x, \mathbf{U}_y, \mathbf{P}, \mathbf{T})^T$ is the column vector of unknown variables, $\mathbf{K}$, the stiffness matrix, represents the diffusion and convection of energy, $\mathbf{F}$, the force vector, incorporates the boundary conditions, and $\mathbf{U}_x$, $\mathbf{U}_y$, $\mathbf{P}$, and $\mathbf{T}$ are the nodal x- and y-components of velocity, pressure, and temperature vectors, respectively. Equation (10) represents the discrete analog of the governing continuum equations for an individual element. The discrete representation for the entire computational domain is obtained through an assembly of all the elemental equations, as well as imposing the continuity of primary (velocity, temperature) and secondary (flux) variables, generating a global system of algebraic equations similar to equation (10).

The consistent penalty method is utilized to effectively eliminate the pressure variable from the governing equations. The continuity, equation (1), is replaced by the equation

$$\frac{\partial u}{\partial x} + \frac{\partial v}{\partial y} = -\varepsilon p \tag{11}$$

which allows a substitution for the pressure variable in the momentum equations. The continuity equation is thus interpreted as a constraint on the velocity degrees of freedom and is satisfied in the approximate sense of equation (11). A value of 10^{-6} was utilized for the penalty parameter ε. Postprocessing of the velocity data recovers the pressure via $p = -\varepsilon^{-1}\nabla \cdot \mathbf{V}$, where $\mathbf{V}$ is the velocity vector.

2.3. Solution techniques

Since the governing equations are only weakly coupled, the global system of momentum and energy equations are solved independently. The non-linearity of the momentum equations requires an iterative technique to obtain a solution whereas the linear energy equation is solved in one iteration. Solution of the two uncoupled problems was found to be quicker than for the single, coupled problem. To assist convergence of the flow field solutions, a composite solution strategy was implemented. The first solution steps (typically four) are performed utilizing the successive substitution method. The nonlinear portions of the governing equations are evaluated using data from the previous iteration, $\mathbf{V}_{N+1} = \mathbf{K}^{-1}(\mathbf{V}_N)\mathbf{F}$. Direct Gaussian elimination is the solution technique utilized in this work.

Upon completion of the successive substitution steps, the Newton–Raphson method is utilized. The solution is linearized using data from the previous iteration according to $\mathbf{V}_{N+1} = \mathbf{V}_N - \mathbf{J}^{-1}(\mathbf{V}_N)\mathbf{R}(\mathbf{V}_N)$, where $\mathbf{J}(\mathbf{V}) = \partial\mathbf{R}/\partial\mathbf{V}$ is the Jacobian matrix of the system of equations $\mathbf{R} = \mathbf{KV} - \mathbf{F}$. The iterations towards the steady state solution are terminated when the two convergence criteria,

$$\left\| 1 - \frac{\mathbf{V}_{N-1}}{\mathbf{V}_N} \right\| \leqslant \delta_v \quad \text{and} \quad \left\| \frac{\mathbf{R}_N}{\mathbf{R}_0} \right\| \leqslant \delta_R, \tag{12}$$

are satisfied. Here $\| \ \|$ is the RMS norm summed over all of the equations, $\mathbf{R}_0$ is the residual computed from the initial solution vector $\mathbf{V}_0$, and the tolerances for the solution and residual vectors, δ_v and δ_R, respectively, were set to 10^{-8}.

A dynamic, relative error based relaxation method is used to increase the convergence rate. The relative error of each degree of freedom, $\|1 - (\Delta_{N-1}/\Delta_N)\|$, $\Delta = \mathbf{U}_x$ or $\mathbf{U}_y$ is used to linearly adjust the relaxation factor from a maximum to a minimum value. During a given iteration the relaxation factors remain fixed throughout the computational domain and are only adjusted between iterations. The relaxation factors for the velocity components typically were adjusted from 0.5–0.1.

For a given geometry, the solution proceeded in several phases. The Reynolds number was first set to its lowest value and the penalized continuity and momentum equations were iteratively solved for the velocity field using the solution of the related Stokes problem as the initial guess ($\mathbf{V}_0$). Then, using this converged velocity solution, the energy equation was solved for each value of obstacle thermal conductivity. The Reynolds number was then incrementally increased and the momentum equations were solved using the previous velocity solution as the initial guess, followed by solutions of the energy equations. This incremental loading strategy provides reasonable initial solution vectors and results in valid solutions at each load step for the desired range of Reynolds numbers.

The present calculations were performed on a highly variable mesh, as shown in Fig. 1(b)–(c). This mesh was designed to capture the sharp gradients and boundary layers near the fluid-solid interfaces and to provide sufficient mesh density at the obstacle surfaces with minimal element distortion. Confirmation of the grid independence of the model required extensive tests to be carried out with increasing mesh densities and various mesh gradings until further refinement showed less than a one percent difference in the results. To eliminate the influences of the entrance and outlet upon the solutions near the physical domain of interest (the obstacle region), additional tests were performed by individually increasing the lengths of the channel before (L_e) and after (L_o) the obstacle. An inlet length of $L_e = 2$ was found to

adequately isolate the obstacle region from any entrance effects. At the highest Reynolds numbers, an outlet length of $L_o = 8$ was necessary to ensure that the large recirculation zone downstream of the obstacle reattached well ahead of the outlet and that the fluid exited the computational domain in a parabolic, fully developed profile. The meshes employed for the various geometries ranged from 214×60 to 274×76. The computations were performed on a Silicon Graphics Indigo2 R10000 workstation. A converged solution required from 600–1200 CPU seconds for the flow field and approximately 10 CPU seconds for the thermal field.

3. Results and discussion

The focus of this work is to examine the influences upon flow and heat transfer to changes in the flow rate and other relevant parameters of a single heated obstacle in a channel. Parametric variations in the obstacle height ($h = 0.125$, 0.25) and width ($w = 0.125$, 0.25, 0.5) yield six different geometries within the channel. Figure 3 shows a scale drawing, relative to the unity channel spacing, of the six cases considered. These geometries were chosen to evaluate the effects of systematic changes in obstacle height, width, size, and shape. The thermal conductivity of the obstacle is varied from that of a thermal insulator ($k_s/k_f = 1$) to other values typical of materials utilized in electronic packages, such as epoxy glass, ceramics, heat spreaders, and encapsulants ($k_s/k_f = 10$–1000), to that of 6061-T6 aluminum ($k_s/k_f = 6600$). The flow rate, characterized by the channel hydraulic diameter based Reynolds number (Re_{D_h}, where $D_h = 2H$), is varied from 200–2000. This range of values is typical of laminar forced convection studies of electronic cooling, where the inlet velocity may range from 0.3 to 5 m s^{-1} [23]. The fixed input parameters utilized in the simulations were $H = 1$, $L_c = 2$, $L_o = 8$, $q'' = 1$, and $Pr = 0.72$.

To validate the numerical scheme used in the present investigation, comparisons with previous studies were performed. This was achieved through adjustments to the model to match the geometric, hydrodynamic, and thermal conditions of the related works. First, comparisons were made with the analytical solutions of Cess and Shaffer [24, 25] to the problems of thermal entry length in a channel with constant wall temperature or heat flux. Calculated entrance region and fully developed Nusselt numbers showed excellent agreement. Next, a hydrodynamic comparison with the single obstacle case of Zebib and Wo [6] was made. Thermal comparisons were not made due to lack of information for their multiconductivity obstacle and the multilayer channel walls with a constant convective coefficient beneath the bottom surface. Their three inlet velocities correspond to $Re_{D_h} = 806$, 1772, and 3222. A comparison of the recirculation zone and reattachment length behind the obstacle was within ~2% for the lowest two Reynolds numbers and within ~8% for the highest (run as laminar flow even though the Reynolds number was well within the transition regime).

A third comparison was made with the study of Davalath and Bayazitoglu [5] for three volumetrically heated obstacles with thermal conductivities $k_s/k_f = 10$, heights = 0.25, widths = 0.5, and spacings = 0.5 in a flow with $200 \leqslant Re_{D_h} \leqslant 3000$. Comparisons between the

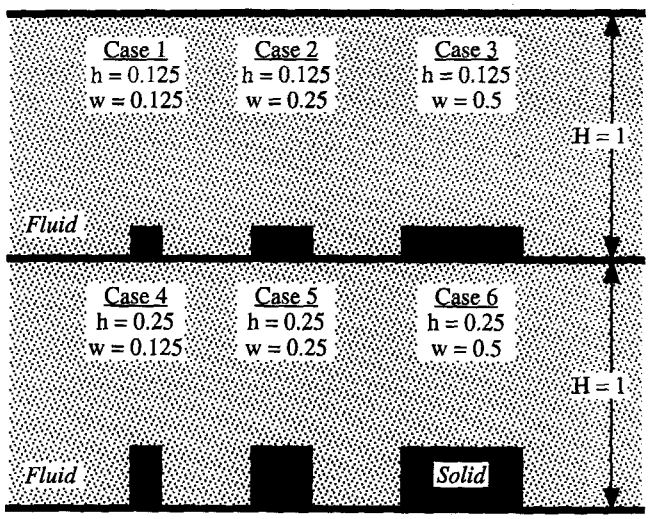

Fig. 2. Comparative scale drawing of the obstacle and channel geometries investigated.

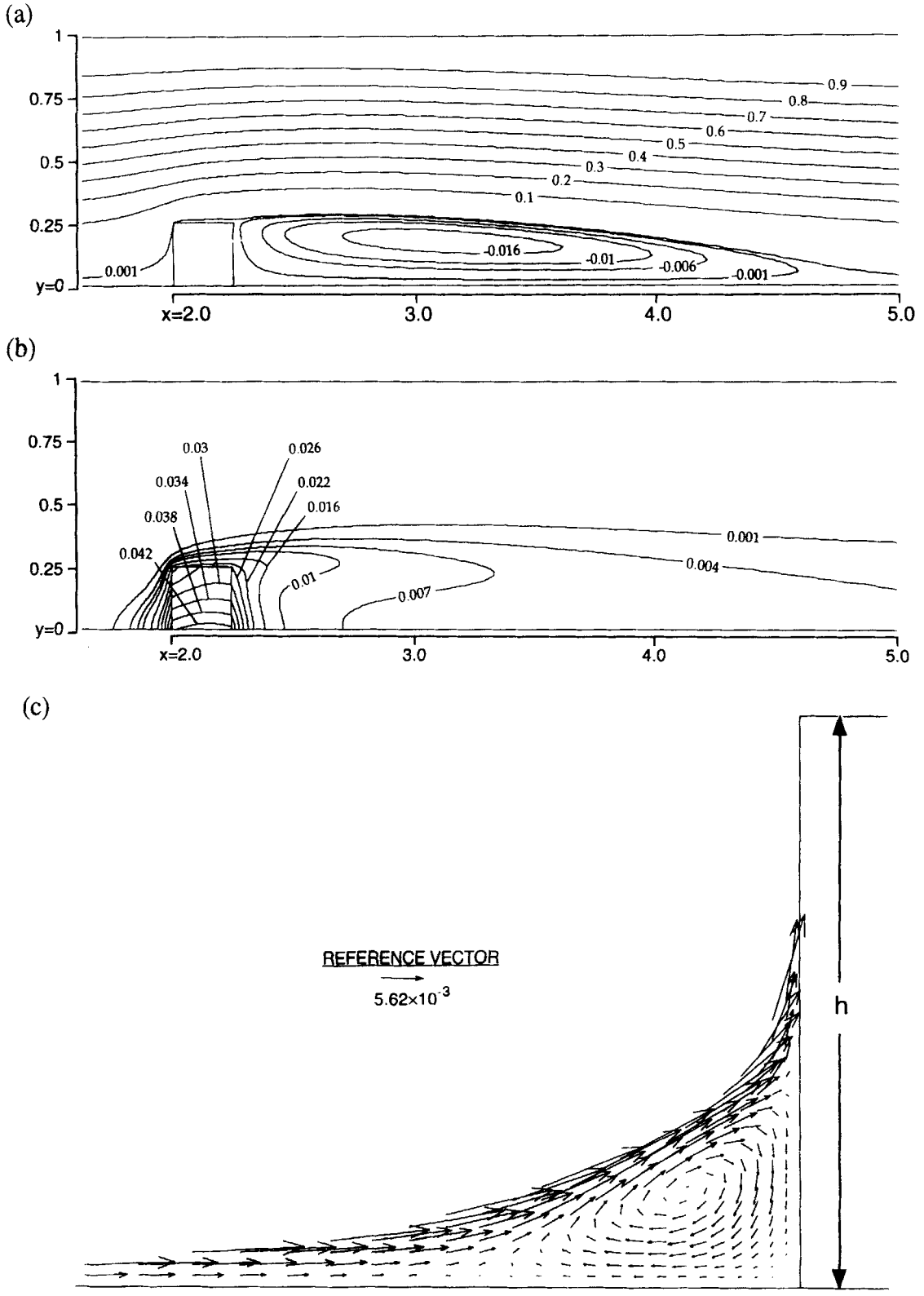

Fig. 3. Flow in a parallel plate channel with a solid, conducting obstacle for $Re_{D_h} = 1000$, $w = 0.25$, $h = 0.25$, and $k_s/k_f = 10$: (a) streamlines, (b) isotherms, and (c) close-up of upstream recirculation zone only showing vectors of the smallest magnitudes.

mean obstacle Nusselt numbers calculated in [5] and the current analysis show discrepancies of up to ~30%. Wall temperature distributions along the obstacle surfaces compare well, but the local Nusselt numbers show noticeable differences. The Nusselt number distributions on the upstream and downstream facing surfaces in [5] show very small, nearly constant values ($0 \leqslant Nu_x \leqslant 2$) compared with those on the upper surfaces ($10 \leqslant Nu_x \leqslant 70$). The current calculations found similar thermal boundary layer development along the upper surfaces. However, Nu_x distributions on the left and right surfaces were found to be dramatically different, with much greater values near the upper corners. This phenomenon has been reported elsewhere, for example [21, 26]. The average Nusselt numbers on the left surface were found to be comparable to those of the top surface while those on the right surface were ~30% of $\overline{Nu}_T$. Utilizing these approximate relationships for $\overline{Nu}_L$ and $\overline{Nu}_R$ with the $\overline{Nu}_T \approx \overline{Nu}_m$ from [5] would allow recalculated mean obstacle Nusselt numbers from [5] to approximately match those found in the current analysis. The mesh in [5] was reported to be 86×42. The mesh utilized for this comparison, 386×66, is far more refined, especially considering that it is a highly variable structure designed to capture near obstacle variations in the flow and thermal fields. This difference in the local mesh system near the obstacles appears to be the reason for the large differentials in mean Nusselt numbers.

To illustrate the results of flow and temperature fields near the obstacle, only this region and its vicinity is presented. However, it should be noted that the computational domain included a much larger region than what is displayed in the subsequent figures. Furthermore, for the sake of brevity, only the main features and characteristics of some of the results are discussed and presented.

The effects of the solid obstacle on the flow and temperature fields are illustrated for a typical case with $Re_{D_h} = 1000$, $w = 0.25$, $h = 0.25$, and $k_s/k_f = 10$. It can be seen in Fig. 3(a) that the presence of the obstacle causes a crowding of the streamlines at the upstream corner (*vena contracta*) as the flow is redirected into the bypass region. Higher Reynolds numbers further compact the streamlines as the fluid forward momentum opposes upward movement into the bypass region. Forward of the lower left corner a very weak clockwise vortex develops, detailed in Fig. 3(c). No upstream recirculation zones were found in [5], perhaps, again, attributable to mesh coarseness. As Re_{D_h} increases the vortex increases in strength as its area increases in the forward and vertical directions. The magnitudes of the velocities within this recirculation, however, are two to three orders of magnitude less than those in the core flow. Downstream, a clockwise recirculation develops extending from approximately four to fourteen obstacle heights down the channel, increasing with Re_{D_h}. Both up and downstream recirculations are similar to those reported by Greenspan [27]. The interactions of the upstream and downstream recirculations with the core flow influences the temperature field, shown in Fig. 3(b). Near the lower corner of the left face the isotherms spread upstream due to the recirculation effect of the corner vortex while near the top left corner the isotherms are crowded by the core flow. These two effects account for increases in the magnitude of the local temperature gradients, directly impacting the local Nusselt number, defined as

$$Nu_x = \frac{h_c H}{k_f} = \frac{-1}{\Theta_w} \frac{\partial \Theta_f}{\partial \mathbf{n}} \tag{13}$$

where the temperature gradient is calculated using a three point finite difference. The Nusselt number distribution on the three obstacle faces for this case is shown in Fig. 4, where the 'Peripheral Distance' axis measures the running total distance moving clockwise from the lower left to lower right corner of the obstacle, as shown in the sketch. The Nusselt number along the left face clearly shows the influences of the lower corner vortex and the fluid impaction near the upper corner.

Beginning at the left corner of the top face a thermal boundary layer develops. Figure 4 compares the top face Nusselt number distribution with an analytical solution [25] to the thermal entrance problem with $q'' = 1$. The analytical solution utilizes the bypass height, $H_b = H - h$, as the appropriate flow height. The analytical Nusselt number distribution, based upon equation (13), is plotted coincident with that of the obstacle top face. At the upper left obstacle corner, equivalent to the entrance of the channel for the analytical solution, the difference between the analytical and numerical Nusselt numbers is largest. This difference decreases moving downstream of the entrance. Near the obstacle upper right corner Nu_x increases slightly. This effect, not seen in the analytical thermal entrance solution, with its infinite channel length and constant q_w, is due to the surface temperature decreasing near the corner where downstream the fluid is not being further heated by the wall. On the downstream obstacle face, Nu_x is large at the upper corner and decreases rapidly to a small, nearly constant value before rising at the bottom corner, where the temperature is greater.

The utility of the analytical solution [25] as an estimate for the Nusselt number along the top face is shown in Fig. 5. Here the analytical and numerical solutions are compared for the extremes in Reynolds number investigated, 200 and 2000, with $q'' = 1$, $w = 0.25$, $h = 0.25$, and $k_s/k_f = 10$. Again, the bypass height $H_b = H - h$ is utilized in the analytical solution. Along the top face the analytical solution substantially overestimates Nu_x near the leading edge, but the difference is small about halfway to the downstream corner. Lehmann and Wirtz [18] experimentally found good agreement between the Graetz solution and the transitional flow results from a channel with two-dimensional, heated ribs. For many

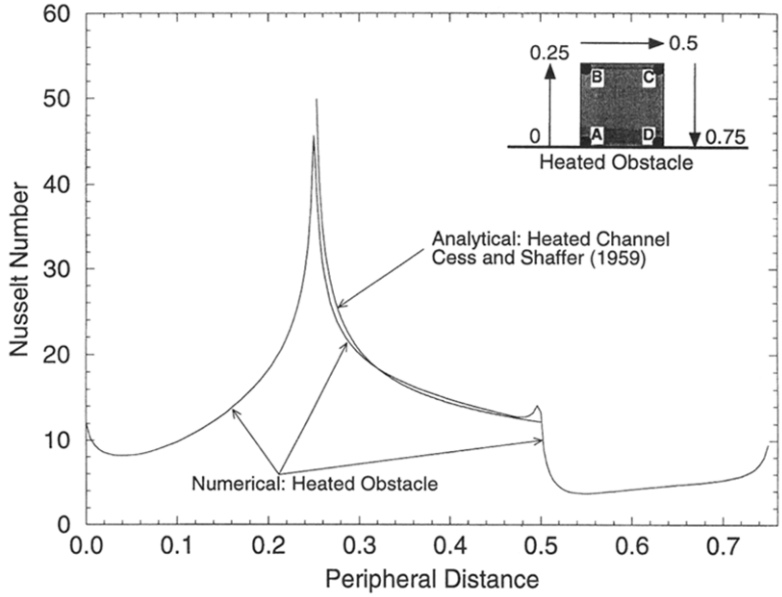

Fig. 4. Local Nusselt number distribution around the three obstacle exposed faces (periphery) compared with an analytical solution [25] for a thermally developing channel flow with $q_w = 1$ and $H_b = 0.75$: Re_{D_h} or $Re_{H_b} = 1000$, $w = 0.25$, $h = 0.25$, and $k_s/k_f = 10$.

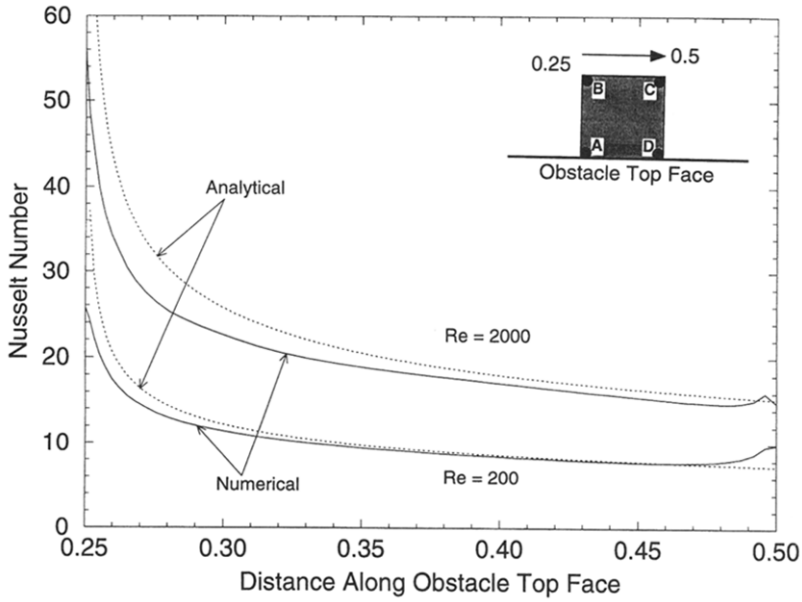

Fig. 5. Comparison of the local Nusselt number distribution on the obstacle top face with that found using an analytical method [25] for the thermally developing channel flow with $q_w = 1$ and $H_b = 0.75$: Re_{D_h} or $Re_{H_b} = 200$ and 2000, $w = 0.25$, $h = 0.25$, and $k_s/k_f = 10$.

geometries the mean Nusselt number along the top face contributes to a significant portion of the heat transfer from the obstacle. The analytical method of Cess and Shaffer [25] can provide an estimate or a comparison for local Nusselt numbers along the top face of an obstacle in forced convective flows when utilizing the proper length scale.

3.1. Effects of the Reynolds number

Figures 6 and 7 show the effects of Reynolds number on the flow field and local Nusselt number for case 5 ($w = 0.25$, $h = 0.25$) with $k_s/k_f = 10$. Comparison of the streamlines for $Re_{D_h} = 200$, 800, 1400, and 2000 in Figure 6 shows that, as Re_{D_h} increases, the length and the relative

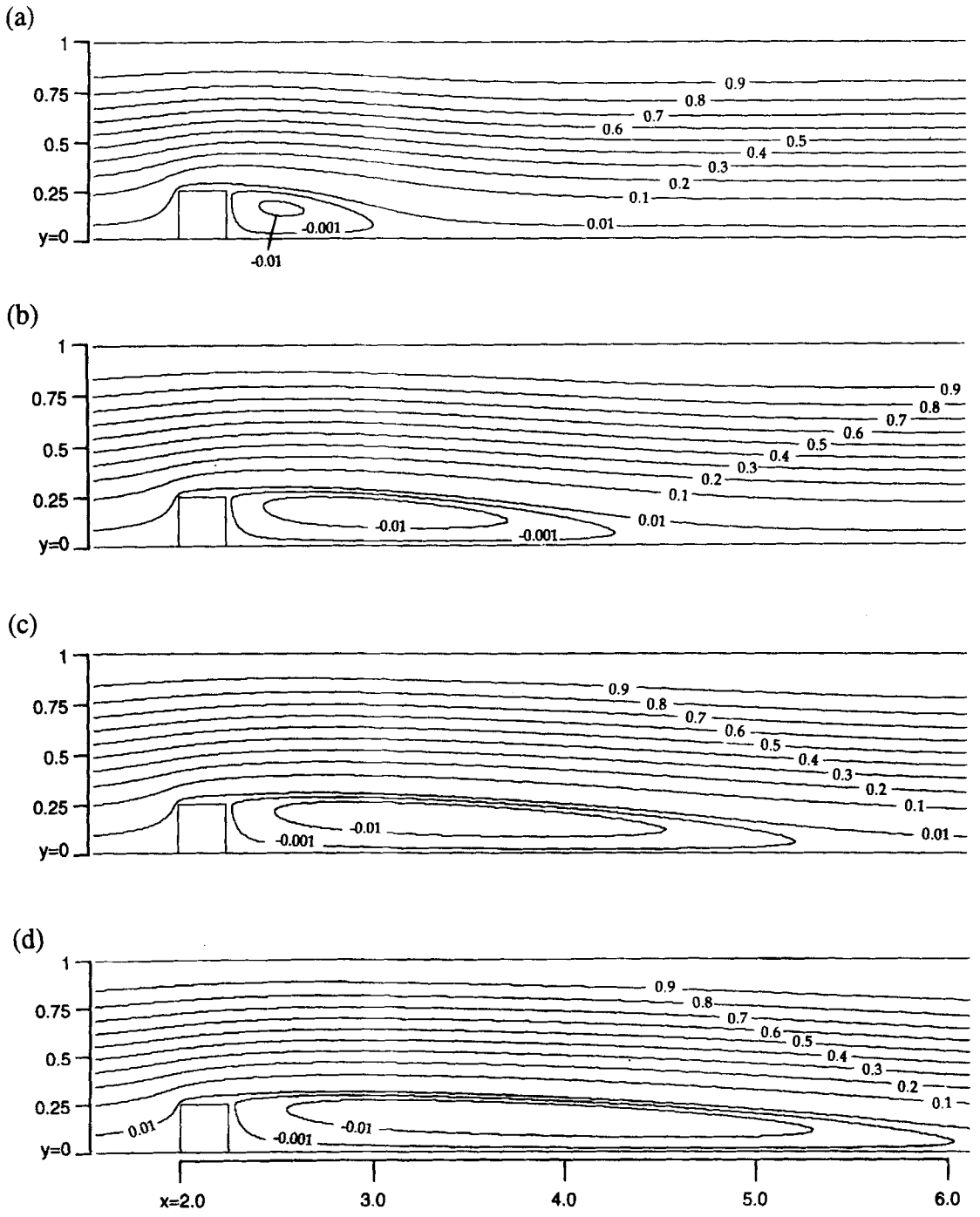

Fig. 6. Effects of the Reynolds number on streamlines for flow in a parallel plate channel with a solid obstacle for $w = 0.25$, $h = 0.25$: (a) $Re_{D_h} = 200$, (b) 800, (c) 1400, and (d) 2000.

strength of the downstream recirculation zone increases. The increased axial momentum of the fluid, caused by the constriction of the bypass region, inhibits its expansion into the full channel downstream of the obstacle. The weak recirculation zone ahead of the obstacle also increases in size and strength with increasing Re_{D_h}. Enlarged views of these recirculations (not shown for brevity) show that the height to which they rise against the obstacle remains nearly constant at about 0.3–0.4 h whereas the forward influence increases from about 0.35–

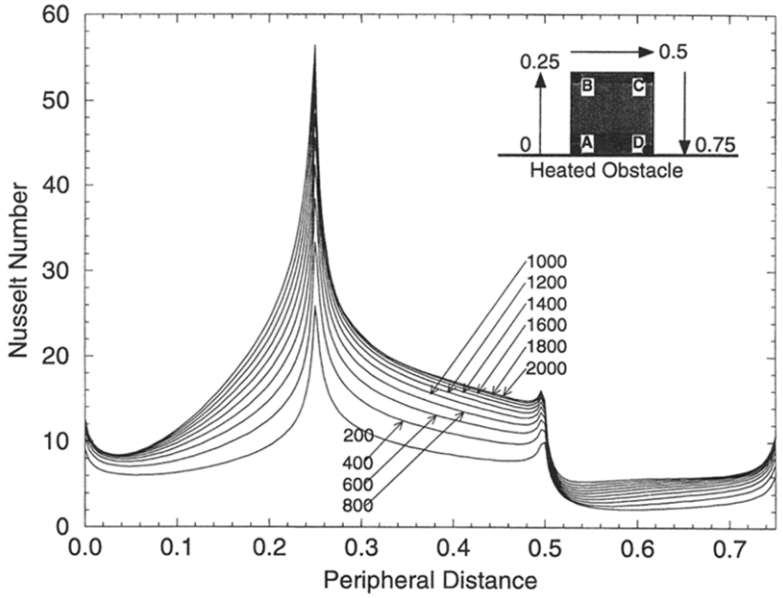

Fig. 7. Effects of Reynolds number variation on local Nusselt number distributions around the obstacle periphery for $w = 0.25$, $h = 0.25$, $k_s/k_f = 10$, and $200 \leqslant Re_{D_h} \leqslant 2000$.

$1.0h$. Again, the velocity magnitudes within this recirculation remain two to three orders of magnitude less than that within the core flow.

The variation of local Nusselt number around the obstacle periphery for $200 \leqslant Re_{D_h} \leqslant 2000$ is shown in Fig. 7. As expected, Nu_x increases with increased Re_{D_h}. Along the left face ($0 \leqslant$ peripheral distance $\leqslant 0.25$) the Nusselt number has a local minimum before rising rapidly near the upper corner. At the lower corner the recirculation and the close proximity of the input heat flux lead to locally large Nu_x values. Near the upstream corner, where increases in flow momentum push the isotherms further back towards the upper portion of the left face (above the recirculation zone), the magnitude of the temperature gradient $|\partial\Theta_f/\partial\mathbf{n}|$ increases. The magnitude of the temperature gradient also increases at the top face when greater flow rates reduce the thickness of the thermal boundary layer. Along the right face ($0.5 \leqslant$ peripheral distance $\leqslant 0.75$) Nu_x increases slightly with increased Re_{D_h}, though the values themselves are small in comparison with those on the top and left faces. As expected, the obstacle surface and maximum temperature decrease with increased Re_{D_h}, the latter being a critical measure towards improving electronic device reliability.

3.2. Effects of the solid thermal conductivity

The thermal conductivity of the obstacle has a large effect upon the heat transfer within the obstacle, as illustrated by the isotherm plots in Fig. 8. Here the obstacle geometry is fixed (case 5: $w = 0.25$, $h = 0.25$) as is $Re_{D_h} = 1000$, but the thermal conductivity is varied from $k_s/k_f = 1$–1000. As the thermal conductivity increases the internal resistance to heat flow is reduced, decreasing the maximum temperature and reducing internal temperature gradients. When the conductivity is two to three orders of magnitude greater than that of the fluid the obstacle is effectively isothermalized, as predicted by the Biot number $\ll 1$ criteria. The corresponding local Nusselt number distributions are shown in Fig. 9. for $k_s/k_f = 1$ the obstacle is a thermal insulator for air flow and the Nu_x shape is considerably different than for $k_s/k_f \geqslant 10$. Near the lower corners of the obstacle, when $k_s/k_f = 1$, both the surface heat flux and temperature are greater with the overall effect being larger Nu_x values. The trend is reversed at the upper corners where both q_w and T_w, and the corresponding Nu_x, are lower than when $k_s/k_f \geqslant 10$. As shown in the inset, when k_s/k_f is increased to 10 or more the variations in surface temperature decrease. For $k_s/k_f \geqslant 100$ the Nu_x distributions are nearly identical. The benefits of increasing obstacle thermal conductivity are reduced temperature gradients within the obstacle and increased surface isothermality, though the returns are diminishing for k_s/k_f greater than about 100.

3.3. Effects of the heating method

The energy production in an obstacle, such as an electronic component, can be approximated as a constant

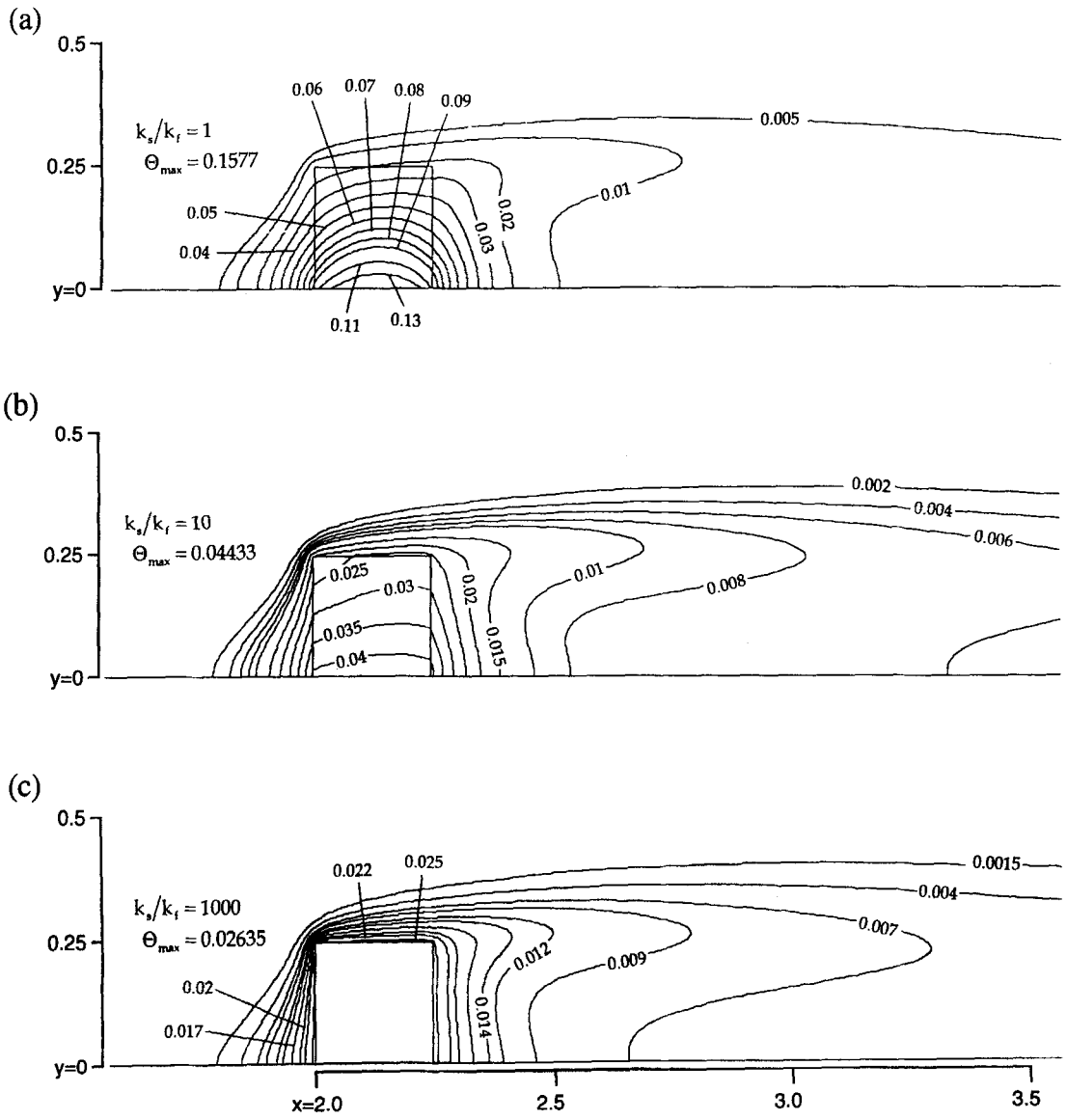

Fig. 8. Effects of the solid thermal conductivity on isotherms for flow in a parallel plate channel with a conducting obstacle for $w = 0.25$, $h = 0.25$, and $Re_{D_h} = 1000$: (a) $k_s/k_f = 1$, (b) 10, and (c) 1000.

surface heat flux or volumetric generation. Both of these approaches have been utilized in previous numerical and experimental investigations. A comparison between these two methods was made for the obstacle of case 5 ($w = 0.25$, $h = 0.25$) with $200 \leqslant Re_{D_h} \leqslant 2000$ and $k_s/k_f = 1$–100. The total energy input into the system was equalized using the balance $q''(w) = q'''(w \times h)$. Comparisons between the known heat input rate, $q_{in} = \int q'' \, dA$ or $\int q''' \, dV$, compare extremely well with the thermal energy leaving the obstacle and entering the fluid, calculated from $q_{out} = \int Nu_x(\mathbf{x})\Theta_w(\mathbf{x}) \, dA$. The energy equation for the solid, equation (5), was modified to include the volumetric source,

$$\left(\frac{k_s}{k_f}\right)\left(\frac{\partial^2 \Theta_s}{\partial x^2} + \frac{\partial^2 \Theta_s}{\partial y^2}\right) + q''' = 0 \tag{14}$$

where the magnitude of the dimensionless source term is $q''' = 1/h$. The only change in boundary conditions is the removal of the constant heat flux at the obstacle bottom surface.

The isotherms in the obstacle region for volumetric heating are shown in Fig. 10 for $w = 0.25$, $h = 0.25$, $Re_{D_h} = 1000$, and $k_s/k_f = 1$, 10, and 100. Compared with the isotherms for a constant surface heat flux (Fig. 8) several differences are apparent. First, the maximum temperatures are lower for volumetric heating, as the energy

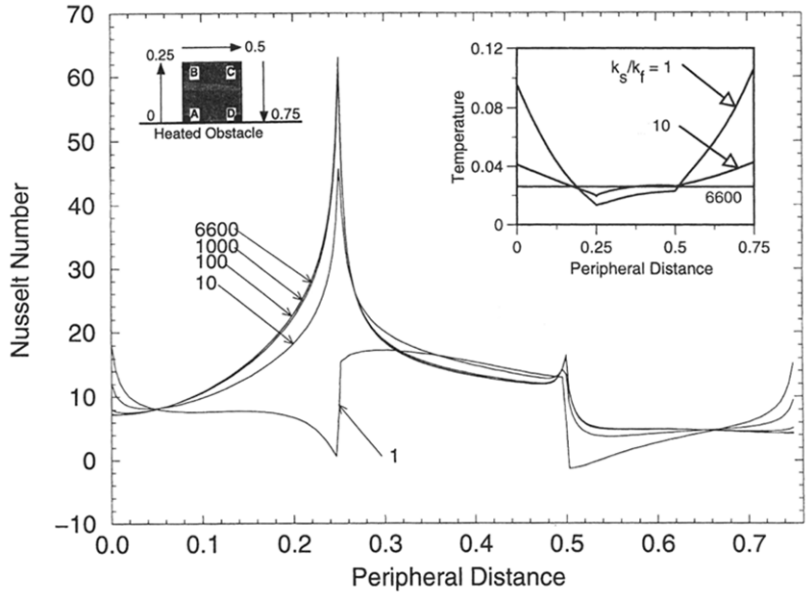

Fig. 9. Effects of variations in thermal conductivity ratio on local Nusselt number distributions around the obstacle periphery for $w = 0.25$, $h = 0.25$, $Re_{D_h} = 1000$, and $1 \leqslant k_s/k_f \leqslant 6600$. The inset shows the obstacle surface temperatures for various k_s/k_f.

input is well distributed within the obstacle compared with bottom surface heating. Second, the regions of maximum temperature are more localized at the bottom center of the obstacle, for $k_s/k_f = 1$ and 10, compared with being spread across the entire base for the surface flux case. Third, larger temperature gradients across the interior of the obstacle exist for volumetric heating as the isotherms are skewed by non uniform local Nusselt numbers. The local Nusselt number distributions for the volumetrically and surface heated cases, not shown for brevity, found that the volumetrically heated obstacle has slightly higher Nu_x values along both the left and right faces except for near the bottom corners where the surface heated obstacles have larger local heat fluxes due to the $q'' = constant$ constraint on the bottom face. Along the top face the Nusselt numbers are nearly identical. Similar behaviors were seen for the entire range of Reynolds numbers and obstacle thermal conductivities investigated. Overall, as expected, little difference in local or mean Nusselt numbers was found whether volumetric generation or a surface heat flux introduced the thermal energy into the obstacle.

3.4. Effects of the obstacle geometry

The set of six obstacle geometries investigated (Fig. 2) can be grouped into four distinct arrangements based upon obstacle width, height, size, and shape. The effect of this geometric ordering will be gauged using mean values of the Nusselt number for the three exposed faces ($\overline{Nu}_L, \overline{Nu}_T, \overline{Nu}_R$) and the overall obstacle mean ($\overline{Nu}_m$). The exposed face Nusselt numbers are calculated using

$$\overline{Nu}_i = \frac{\int_{A_i} Nu_x \, dx}{A_i} \tag{15}$$

where A_i is the exposed area of interest. The thermal conductivity was fixed at $k_s/k_f = 1000$ for the following comparisons while the Reynolds number varied from 200–2000.

The effects of varying the obstacle width is demonstrated by comparing cases with a fixed height. The greatest effect is in the top face mean Nusselt number, shown in Fig. 11 for cases 4, 5, and 6 where $w = 0.125$, 0.25 and 0.5 and $h = 0.25$. The value of $\overline{Nu}_L$ is seen to change very little and $\overline{Nu}_R$ decreases slightly with increasing width. Increasing the width of the top face decreases the value of $\overline{Nu}_T$ by nearly 30% as a larger portion of the face is further from the entrance plane and experiences lower values of Nu_x. Since the obstacle mean Nusselt number is an area weighted average of those of the three exposed faces, the values of $\overline{Nu}_m$ change only slightly with increases in width. This suggests that for evenly distributed heat sources encased in materials of good thermal conductivity, the width of the object is not critical. However, highly localized heat sources would benefit from placement near the top face for slender obstacles or near the left face, which experiences consistently high $\overline{Nu}_L$ values irrespective of obstacle width. Similar results were found for cases 1, 2 and 3 where $w = 0.125$ to 0.5 and $h = 0.125$.

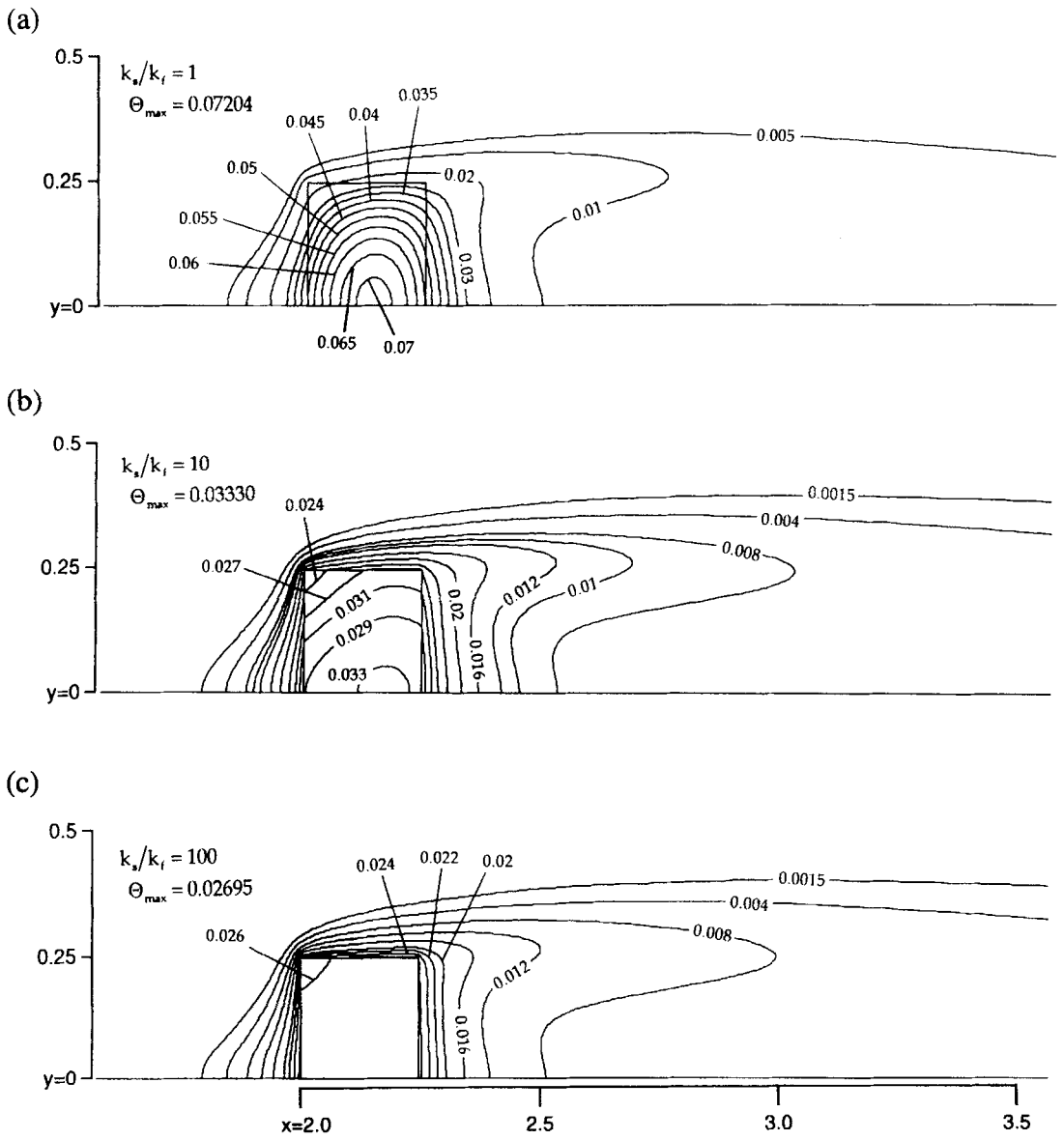

Fig. 10. Effects of the solid thermal conductivity on isotherms for flow in a parallel plate channel with a volumetrically heated obstacle for $w = 0.25$, $h = 0.25$, and $Re_{D_h} = 1000$: (a) $k_s/k_f = 1$, (b) 10, and (c) 100.

Figure 12 presents the changes in mean Nusselt numbers as the obstacle height increases from 0.125–0.25 for a fixed width of 0.25 (cases 2 and 5). Again, the values of $\overline{Nu}_R$ only differ slightly and, as Re_{D_h} increases, become nearly equal. This is because directly behind the obstacle the dominant heat transfer mechanism is the recirculation, which in the immediate downstream region is only slightly affected by changes in height or flow rate. For all the exposed obstacle faces increases in height increase the internal thermal resistance, leading to decreases in heat transfer, though the effect is most pronounced for $\overline{Nu}_L$ and $\overline{Nu}_T$. This produces a similar trend for $\overline{Nu}_m$ where, at the highest Re_{D_h}, the taller obstacle has a $\overline{Nu}_m$ decrease of about 20%. In the other sets of fixed width-variable height cases, similar trends are seen. Thus, reductions in the overall obstacle mean Nusselt number are found as the height is increased and as the width is increased. If the thermal energy flux within an obstacle, such as the waste heat generated within an electronic component, can be held constant, division into smaller units will yield higher mean Nusselt numbers. This is analogous to transforming a large obstacle into a set of 'fins' composed of smaller obstacles.

The effects of an increase in obstacle size, that is keep-

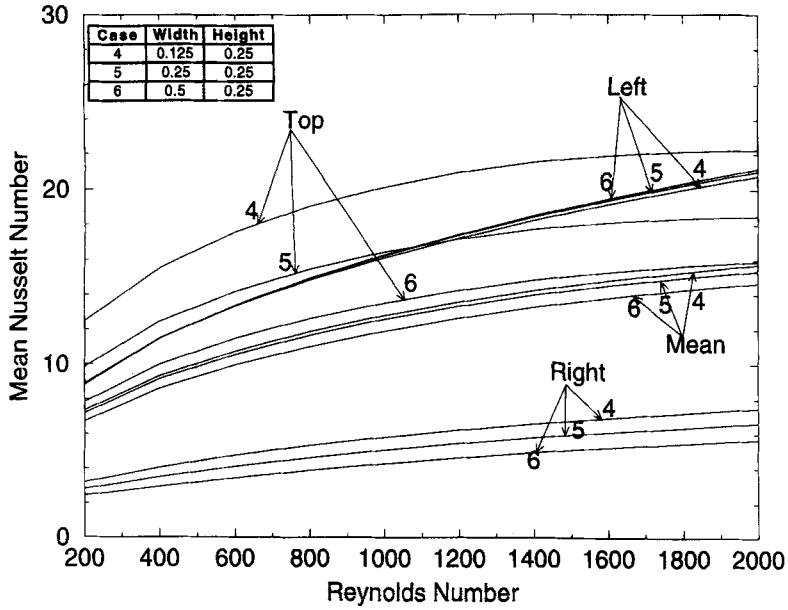

Fig. 11. Effects of obstacle width variations on mean and exposed face mean Nusselt numbers versus Reynolds number for case 4 ($w = 0.125$, $h = 0.25$), case 5 ($w = 0.25$, $h = 0.25$), and case 6 ($w = 0.5$, $h = 0.5$) with $k_s/k_f = 1000$.

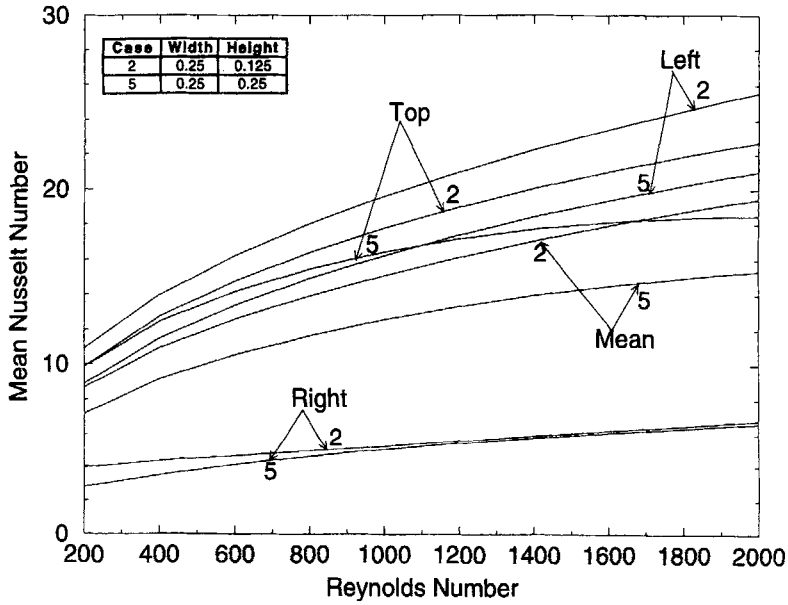

Fig. 12. Effects of obstacle height variations on mean and exposed face mean Nusselt numbers versus Reynolds number for case 2 ($w = 0.25$, $h = 0.125$) and case 5 ($w = 0.25$, $h = 0.25$) with $k_s/k_f = 1000$.

ing the obstacle aspect ratio constant at $w/h = 1$ and increasing the volume, was found by comparing the results for case 1 ($w = h = 0.125$) to case 5 ($w = h = 0.25$). For the range of Re_{D_h} investigated the three exposed face mean Nusselt numbers and the obstacle mean value decreased as the size was increased. At $Re_{D_h} = 2000$, the $\overline{Nu}_m$ for case 5 is over 20% lower than that for case 1, whereby $\overline{Nu}_L$ is about 15% less and $\overline{Nu}_T$ about 35% lower. In this study the smaller obstacle introduces less thermal energy into the channel due to its smaller constant heat flux surface and has a lower internal thermal resistance. This reduces both the obstacle surface

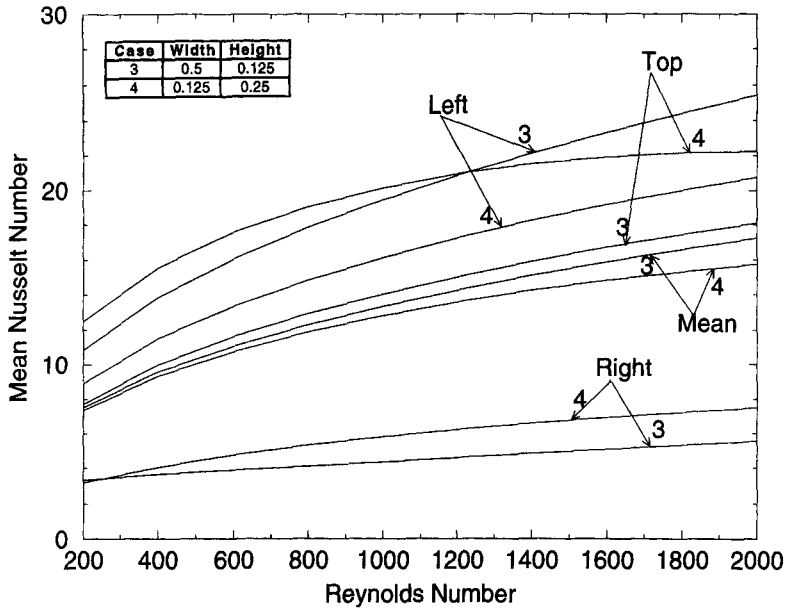

Fig. 13. Effects of obstacle shape variations on mean and exposed face mean Nusselt numbers versus Reynolds number for case 3 ($w = 0.5$, $h = 0.125$) and case 4 ($w = 0.125$, $h = 0.25$) with $k_s/k_f = 1000$.

temperature and the thermal boundary layer penetration into the fluid, consequently increasing the mean Nusselt numbers.

The largest difference in obstacle shape is between case 3 (low-wide) and case 4 (tall-slender). $\overline{Nu}_L$ for case 3 is larger than for case 4 at all Re_{D_h}, as shown in Fig. 13. This is due to the larger forward recirculation zone and its correspondingly lower Nu_x for the taller left face of case 4. Along the top face, however, $\overline{Nu}_T$ for case 4 is greater as a larger percentage of its face is in the initial region of the thermal boundary layer compared with a wider obstacle where a considerable portion of the surface is downstream of the entry and experiencing lower local Nusselt numbers. Along the right face the tall obstacle experiences somewhat larger $\overline{Nu}_R$ values. The obstacle mean Nusselt number is a balance of these effects such that the low-wide (case 3) obstacle has a slight advantage in $\overline{Nu}_m$, about 10% larger, at the highest Reynolds numbers. Due to this similarity in $\overline{Nu}_m$ the two geometries would offer similar heat transfer characteristics for well distributed heat sources, while the top face of the tall-slender obstacle offers slightly better mean Nusselt numbers at lower Re_{D_h} and the left face of the low-wide obstacle offers the highest mean Nusselt numbers for larger Re_{D_h}. Therefore, the thermal energy transport from highly localized heat sources could be optimized with proper placement in these geometries.

Correlations for the obstacle mean Nusselt numbers were developed using the obtained numerical results. Two equations are presented: one to be used for an individual geometry and a second incorporating the entire parametric database. Equation (16) was developed for the individual cases shown in Fig. 2.

$$\overline{Nu}_m = a Re_{D_h}^b \left(\frac{k_s/k_f}{c + k_s/k_f} \right). \tag{16}$$

As the geometry of an individual case is fixed, $\overline{Nu}_m = f(Re_{D_h}, k_s/k_f)$ and six sets of parameters are required for the six cases. The values of a, b, and c are given in Table 1 for each case. Equation (16) was found to fit the data for the individual six cases with mean percent differences of $\leqslant 2.5\%$ while having correlation coefficients from 0.984 to 0.994. The second correlation attempts to reduce to a single equation the results incorporating the complete range of parametric variables: $200 \leqslant Re_{D_h}$

Table 1.
Values of the parameters for the mean Nusselt number correlations developed from the numerical results for flow in a parallel plate channel with a solid, conducting obstacle

Case(s)	Equation	a	b	c	d
1	16	1.6514	0.3311	0.2828	
2	16	1.3647	0.3501	0.0788	
3	16	1.0956	0.3650	−0.0336	
4	16	1.4842	0.3102	0.9326	
5	16	1.4537	0.3112	0.4404	
6	16	1.2802	0.3229	0.1691	
1, 2, 3	17	1.5164	0.3471	0.1081	−0.4079
4, 5, 6	17	1.3951	0.3144	0.4538	0.0278

$\leqslant 2000$, $0.125 \leqslant w \leqslant 0.5$, $0.125 \leqslant h \leqslant 0.25$, and $1 \leqslant k_s/k_f \leqslant 6600$. It was found that the correlation must be bifurcated about the obstacle height to provide a good fit with the numerical results. The resulting equation

$$\overline{Nu}_m = a Re_{D_h}^b \left(\frac{k_s/k_f}{c + k_s/k_f}\right)(1+w)^d \tag{17}$$

utilizes different values of the constants a–d whether the height is 0.125 (cases 1–3) or 0.25 (cases 4–6), as given in Table 1. Equation (17) was found to fit cases 1–3 and 4–6 with correlation coefficients of 0.952 and 0.927 and mean percent differences of 3.9% and 5.5%, respectively. The value of the Reynolds number exponent in the correlations was found to not vary much for the range of parameters investigated, as reported in other investigations.

4. Conclusions

An extensive investigation of the fluid flow and heat transfer in a parallel plate channel with a solid, conducting obstacle is presented in this work. Parametric numerical simulations have been performed to capture the fundamental and practical results. The rectangular obstacle changes the parabolic velocity field significantly, resulting in recirculation zones both up- and downstream and a thermal boundary layer along the top face. The dependence of flow and temperature fields on parametric changes in the governing parameters, Reynolds number, solid thermal conductivity, heating method, and two geometric parameters, is documented. The results of this investigation show that the shape and material of the obstacle has a significant effect on the fluid flow and heat transfer. An analytical solution was found to provide a reasonable estimate for the Nusselt number on the top face of the obstacle if the bypass height was utilized to characterize the flow. Little difference in Nusselt numbers was found when the thermal energy is introduced through volumetric generation or a surface heat flux. Correlations, developed for the obstacle mean Nusselt numbers as functions of the parametric variables, were found to describe the numerical results with mean errors less than six percent.

Acknowledgement

The support of the Aerospace Power Division of the USAF Wright Laboratory under contract F3360196MT565 is acknowledged and appreciated.

References

[1] Bar-Cohen A. State-of-the-art and trends in the thermal packaging of electronic equipment. Journal of Electronic Packaging 1992;114:257–270.

[2] U.S. Department of Defense, Reliability Prediction of Electronic Equipment. Military Handbook MIL-HDBK-217F, Chap. 6, Washington, DC, 1991.

[3] Incropera FP. Convection heat transfer in electronic equipment cooling. Journal of Heat Transfer 1988;110:1097–1111.

[4] Haji-Sheikh A. Peak temperature in high-power chips. IEEE Transactions on Electron Devices 1990;37:902–907.

[5] Davalath J, Bayazitoglu Y. Forced convection cooling across rectangular blocks. Journal of Heat Transfer 1987;109:321–328.

[6] Zebib A, Wo YK. A two-dimensional conjugate heat transfer model for forced air cooling of an electronic device. Journal of Electronic Packaging 1989;111:41–45.

[7] Nigen JS, Amon CH. Effect of material composition and localized heat generation on time-dependent conjugate heat transport. International Journal of Heat and Mass Transfer 1995;38:1565–1576.

[8] Huang PC, Vafai K. Analysis of forced convection enhancement in a channel using porous blocks. Journal of Thermophysics and Heat Transfer 1994;8:249–259.

[9] Moffat RJ, Ortega A. Direct air cooling electronic components. In Advances in Thermal Modeling of Electronic Components and Systems, ed. Bar-Cohen A. and Kraus A. D. Vol. 1, Chap. 3. Hemisphere, New York 1988.

[10] Yang YT, Yang S. Numerical study of turbulent flow in two-dimensional channel with surface mounted obstacle. International Journal of Heat and Mass Transfer 1994;37:2985–2991.

[11] Wietrzak A, Poulikakos D. Turbulent forced convective cooling of microelectronic devices. International Journal of Heat and Fluid Flow 1990;11:105–113.

[12] Choi CY, Kim SJ, Ortega A. Effects of substrate conductivity on convective cooling of electronic components. Journal of Electronic Packaging 1994;116:198–205.

[13] Jubran BA, Swiety SA, Hamdan MA. Convective heat transfer and pressure drop characteristics of various array configurations to simulate the cooling of electronic modules. International Journal of Heat and Mass Transfer 1996;39:3519–3529.

[14] Sparrow EM, Niethammer JE, Chaboki A. Heat transfer and pressure drop characteristics of arrays of rectangular modules encountered in electronic equipment. International Journal of Heat and Mass Transfer 1982;25:961–973.

[15] Sparrow EM, Yanezmoreno AA, Otis DR. Convective heat transfer response to height differences in an array of block-like electronic components. International Journal of Heat and Mass Transfer 1984:27:469–473.

[16] Nakayama W, Park SH. Conjugate heat transfer from a single surface-mounted block to forced convective air flow in a channel. Journal of Heat Transfer 1996;118:301–309.

[17] Roeller PT, Stevens J, Webb BW. Heat transfer and turbulent flow characteristics of isolated three-dimensional protrusions in channels. Journal of Heat Transfer 1991;113:597–603.

[18] Lehmann GL, Wirtz RA. The effect of variations in streamwise spacing and length on convection from surface mounted rectangular components. Journal of Electronic Packaging 1989;111:26–32.

[19] Garimella SV, Eibeck PA. Heat transfer characteristics of

an array of protruding elements in single phase forced convection. International Journal of Heat and Mass Transfer 1990;33:2659–2669.

[20] Vafai K, Kim SJ. Analysis of surface enhancement by a porous substrate. Journal of Heat Transfer 1990;112:700–705.

[21] Kim SY, Sung HJ, Hyun JM. Mixed convection from multiple-layered boards with cross-streamwise periodic boundary conditions. International Journal of Heat and Mass Transfer 1992;35:2941–2952.

[22] FIDAP, Theory Manual. Fluid Dynamics International, Evanston, IL, 1993.

[23] Anderson AM, Moffat RJ. The adiabatic heat transfer coefficient and the superposition kernel function: Part 1—Data for arrays of flatpacks for different flow conditions. Journal of Electronic Packaging 1992;114:14–21.

[24] Cess, RD, Shaffer EC. Summary of laminar heat transfer between parallel plates with unsymmetrical wall temperatures. Journal of Aero Space Sciences 1959;26:538.

[25] Cess RD, Shaffer EC. Heat transfer to laminar flow between parallel plates with a prescribed wall heat flux. Applied Scientific Research 1959:A8:339–344.

[26] Kang BH, Jaluria Y, Tewari SS. Mixed convection transport from an isolated heat source module on a horizontal plate. Journal of Heat Transfer 1990;112:653–661.

[27] Greenspan D. Numerical studies of steady, viscous, incompressible flow in a channel with a step. Journal of Engineering Mathematics 1969:3:21–28.